Available online at www.sciencedirect.com

ScienceDirect

Procedia Engineering 185 (2017) 1 – 8

Procedia Engineering

www.elsevier.com/locate/procedia

6th Russian-German Conference on Electric Propulsion and Their Application

Advanced electric propulsion diagnostic tools at IOM

C. Bundesmann[a,*], C. Eichhorn[a], F. Scholze[a], D. Spemann[a], H. Neumann[a], F. Scortecci[b], H.J. Leiter[c], K. Holste[d], P.J. Klar[d], A. Bulit[e], K. Dannenmayer[e], J. Gonzalez del Amo[e]

[a] *Leibniz-Institute of Surface Modification, Permoserstr. 15, 04318 Leipzig, Germany*
[b] *Aerospazio Tecnologie s.r.l., Via Provinciale Nord 42a, 53040 Rapolano Terme, Siena, Italy*
[c] *Airbus Defence & Space GmbH, Im Langen Grund, 74239 Hardthausen-Lampoldshausen, Germany*
[d] *Justus-Liebig-Universität Gießen, Heinrich-Buff-Ring 16, 35392 Gießen, Germany*
[e] *ESA/ESTEC, Keplerlaan 1, 2201 AZ Noordwijk, The Netherlands*

Abstract

Recently, we have set up an Advanced Electric Propulsion Diagnostic (AEPD) platform [1], which allows for the in-situ measurement of a comprehensive set of thruster performance parameters. The platform utilizes a five-axis-movement system for precise positioning of the thruster with respect to the diagnostic heads. In the first setup (AEPD1) an energy-selective mass spectrometer (ESMS) and a miniaturized Faraday probe for ion beam characterization, a telemicroscope and a triangular laser head for measuring the erosion of mechanical parts, and a pyrometer for surface temperature measurements were integrated. The capabilities of the AEPD1 platform were demonstrated with two electric propulsion thrusters, a gridded ion thruster RIT 22 (Airbus Defence & Space, Germany, [1 3]) and a Hall effect thruster SPT 100D EM1 (EDB Fakel, Russia, [1,4]), in two different vacuum facilities.

Peer-review under responsibility of the scientific committee of the 6th Russian-German Conference on Electric Propulsion and Their Application

Keywords: electric propulsion, diagnostic tools.

1. Introduction

Despite the successful verification of the potential of the AEPD1 platform, the tests revealed some severe problems. Firstly, the dimension of some of the diagnostic heads is in the order of the size of the exit plane of the tested thrusters. Thus, the interaction of diagnostic heads and energetic particle beam is rather large. Secondly, some of the diagnostic heads were placed inside vacuum sealed housings equipped with appropriate windows for safety reasons. Because of this, there is a certain risk that the window might break, when the housing is brought into the energetic particle beam. Breaking the window would result in a vacuum breakdown with the severe danger that the thruster or other devices might get damaged.

In order to overcome these problems, we are currently testing a new setup (AEPD2) [5,6], which utilizes modified (telemicroscope, triangular laser head), alternative (pyrometer) or additional diagnostic heads (thermocamera, retarding potential analyser) [7].

* Corresponding author. Tel.: + 493412353354;
E-mail address: carsten.bundesmann@iom-leipzig.de

Peer-review under responsibility of the scientific committee of the 6th Russian-German Conference on Electric Propulsion and Their Application
doi:10.1016/j.proeng.2017.03.283

The goal is to operate all diagnostic heads in vacuum. Doing so, we can reduce the dimension of the diagnostic heads considerably and eliminate the risk of a vacuum breakdown. Furthermore, the new diagnostic heads extend the variety of implemented measurement techniques (thermal imaging with thermocamera) or provide a low-cost alternative to existing devices (retarding potential analyser instead of the ESMS). Here, we describe the design of the diagnostic heads developed at the Leibniz-Institute of Surface Modification (IOM) and present the first experimental results, exemplary, with a gridded ion thruster RIT-µX.

The AEPD2 platform can also be equipped with an ExB probe, active thermal probe or Faraday probe developed, partly, by project partners. More information on these probes and their performance are given in References [5,6].

2. Experimental

2.1 Telemicroscope

The telemicroscope is used for high-resolution optical imaging. Taking images allows measuring, for instance, the erosion of mechanical parts [2,4]. The telemicroscope consists of a CCD camera, an extension tube and a photographic lens. The first setup of the telemicroscope was used a vacuum-sealed housing, because the CCD camera was not specified for in-vacuum operation, with a shutter and high-power LEDs for illumination. The setup worked fine [1,2,4] but the dimension was rather large: 120 mm in diameter and 500 mm in length.

In order to overcome the problems outlined above (size, vacuum breakdown), we decided to redesign the setup Fig. 1). First of all, the telemicroscope should be operated in-vacuum, even though it is still not specified for in-vacuum operation. Because of that, a smaller housing, which does not need to be vacuum-sealed, could be used. Furthermore, a smaller photographic lens is used. In order to select the best setup, calculations using simple optics and principal performance tests were done.

Imaging (see Fig. 2) can be described by the lens equation:

$$\frac{1}{f} = \frac{1}{s_1} + \frac{1}{s_2}$$

Here s_1 and s_2 denote the object distance and the image distance, respectively.

The magnification M can be calculated by

$$M = \frac{w_2}{w_1} = \frac{h_2}{h_1} = \frac{s_2}{s_1}$$

w_i and h_i are the width and height, respectively, of the object (i = 1) and image (i = 2).

First the case that the distance between object and camera is infinite, i.e. $s_1 = \infty$ is considered. In order to get a sharp image, the image plane must be placed at the focal point of the lens, i.e. $s_2 = f$.

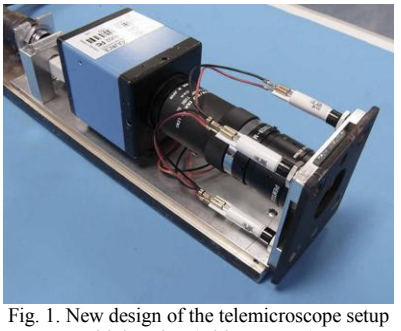

Fig. 1. New design of the telemicroscope setup with housing (without cover)

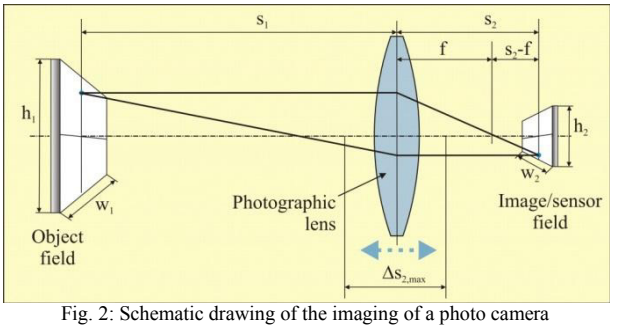

Fig. 2: Schematic drawing of the imaging of a photo camera (telemicroscope)

If the distance between object and camera is finite, the distance between lens and imaging plane must be increased by

$$\Delta s_2 = s_2 - f = \frac{1}{\frac{1}{f} - \frac{1}{s_1}} - f = \frac{f^2}{s_1 - f}$$

in order to get a sharp image. The magnification M is now

$$M = \frac{s_2 - f}{f}$$

The width and the height of the object field, which is focused on the sensor (image size), can be calculated by

$$w_1 = \frac{w_2}{M} = w_2 \frac{f}{s_2 - f} = w_2 \frac{s_1 - f}{f}$$

$$h_1 = \frac{h_2}{M} = h_2 \frac{f}{s_2 - f} = h_2 \frac{s_1 - f}{f}$$

If the sensor is divided into $m_w \times m_h$ pixels, each pixel corresponds to a section of the object plane with the width and the height of

$$w_1^{pix} = \frac{w_1}{m_w} = \frac{w_2}{m_w} \frac{f}{s_2 - f} = \frac{w_2 (s_1 - f)}{m_w f}$$

$$h_1^{pix} = \frac{h_1}{m_h} = \frac{h_2}{m_h} \frac{f}{s_2 - f} = \frac{h_2 (s_1 - f)}{m_h f}$$

entire sensor plane.

Fig. 3 shows an exemplary, calculated and measured results for a setup with a lens with a focal length of $f = 50$ mm and different extension tube lengths. There is excellent agreement between the calculated and measured data. The goal was to have a setup, which is as small as possible and has a lateral resolution of better than 10 µm. Therefore, we chose the lens with $f = 50$ mm and an extension tube the length of 40 mm.

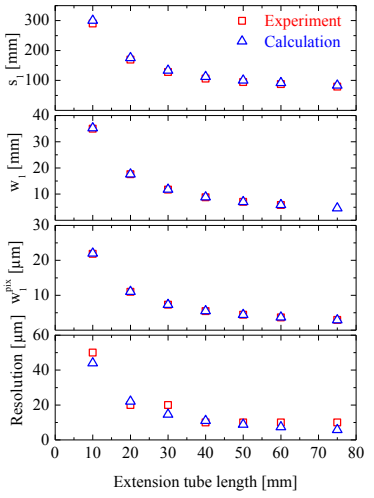

Fig. 3: Measured (red squares) and calculated (blue triangles) performance data versus extension tube length of the telemicroscope: working distance s_1, total horizontal field of view w_1, horizontal field of view per pixel w_1^{pix}, and lateral resolution. The focusing length is f = 50 mm

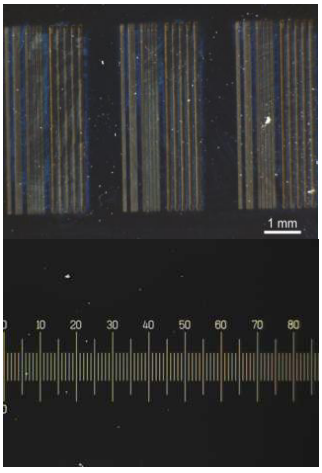

Fig. 4. Telemicroscope image of the test structure for verifying the lateral resolution (left) and field of view (right)

The camera extension tube and lens are commercially available. However, some vacuum-sensitive electronic parts (capacitors) had to be replaced. The resolution of the CCD camera is 1600 pixel x 1200 pixel. The overall dimension (including housing) is 60 x 70 x 210 mm^3. A sapphire window is used to protect the optics from direct particle impingement, because sapphire is known to be very hard. There are also four high-power LEDs for illumination.

The performance of the telemicroscope was investigated using two test structures: a graticule structure for determining the field of view (see Reference [6]) and a special line structure for verifying the achievable resolution. Both test structures are shown in Fig. 4. The first structure consists of several pairs of lines. Each pair has five lines

with equal width and spacing ranging from 10 µm up to 100 µm. It can be seen in Fig. 4 that all pairs of lines down to 10 µm can be resolved. Hence the lateral resolution of the telemicroscope is better than 10 µm. In summary, performance evaluation revealed the following parameters: image size (field of view) is 8.75 x 6.56 mm^2 at a working distance of 112.5 mm, lateral (radial) accuracy is better than 0.01 mm, and depth of field (axial resolution) is better than 0.5 mm.

2.2 Triangular laser head

The triangular laser head measures the distance to an object upon exploitation of the triangulation effect (see Fig. 5). When scanning across an object of interest, the surface profile can be determined, which gives access to axial (and lateral) erosion.

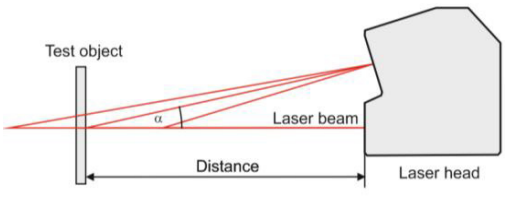

Fig. 5. Sketch of the measurement principle of the triangular laser head (triangulation effect)

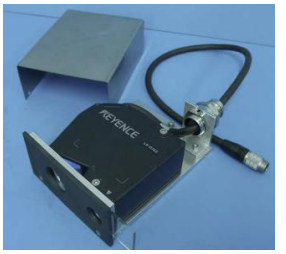

Fig. 6. Triangular laser head setup with housing

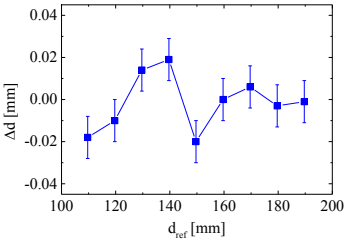

Fig. 7. Difference between set distance and distance measured with the triangular laser head

Similar to the telemicroscope, the triangular laser head was also placed inside a vacuum-sealed housing when used with the AEPD1 platform. The housing contained not only the triangular laser head but also the pyrometer. The diameter and length of the housing was about 200 mm and 300 mm, respectively. That was almost the same as the diameter of the extraction grid system of the gridded ion thruster RIT-22.

Again, now the triangular laser head should be operated in-vacuum. Fig. 6 shows the new design with a considerably smaller housing (not vacuum-sealed) with two sapphire windows.

The triangular laser head is a commercial device. Again, some vacuum-sensitive electronic parts had to be replaced. The distance measurement range covers 110 mm - 190 mm with a specified repeatability of better than 0.001 mm and distance resolution of better than 0.01 mm. The spot size is about 0.2 mm at a distance of 150 mm. The overall dimension of the setup (including housing) is 95 x 47 x 127 mm^3.

We performed principal tests of the triangular laser head using a high-precision linear table. The table was moved to certain positions. Then the measured distance is compared to the relative position (change) of the linear table. The results are plotted in Fig. 7. The data show that the error bar is about 0.02 mm.

2.3 Pyrometer

The pyrometer is used to perform temperature spot measurements or line scans. The measurement principle is based on Planck's law,

$$B_\lambda(T,\varepsilon,\lambda) = \varepsilon \cdot t \cdot \frac{2 \cdot h \cdot c^2}{\lambda^5} \cdot \frac{1}{exp\left(\frac{h \cdot c}{\lambda \cdot k \cdot T}\right) - 1}$$

i.e. the intensity of the emitted infrared radiation B_λ depends on the object temperature T, the emissivity ε of the object material, the wavelength λ (and, if needed, the transmission t of a window). h, c and k are Planck constant, speed of light and Boltzmann constant, respectively.

The old setup was rather large. Therefore, we decided to use an alternative, much smaller device and operate it in-vacuum. The pyrometer sensor head including housing is shown in Fig. 8. The pyrometer is a commercial device. Due to the in-vacuum operation, some vacuum-sensitive electronic parts had to be replaced or removed. A sapphire window is used in order to protect the pyrometer optics from erosion due to energetic particle impingement.

Sapphire has good mechanical hardness as well as high transmission at the wavelength of the pyrometer ($t \sim 0.85$ at $\lambda = 2.3$ µm, see Fig. 8).

Fig. 8. Pyrometer sensor head with housing

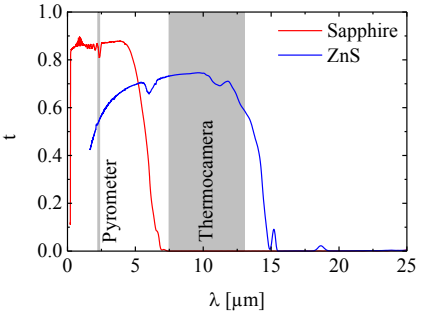

Fig. 9. Measured transmission of the sapphire window for the pyrometer (red line) and the ZnS window for the thermocamera (blue line)

The pyrometer operates at a wavelength of 2.3 µm. The spot size is 1.5 mm at the focal distance of 110 mm. Temperature range and resolution are 150°C – 1000°C and 0.1°C, respectively. The system accuracy and repeatability are given to be 0.3 % of reading + 2°C and 0.1 % of reading + 1°C, respectively. The overall dimension (including housing) is 25 x 30 x 47 mm^3.

2.4 Thermocamera

The thermocamera takes temperature images of objects of interest. As for the pyrometer, its operation is based on principles described by Planck's law. The thermocamera uses a focal plane array as detector, which allows taking images. In the AEPD1 platform a thermocamera was tested by project partners. The thermocamera was placed outside of the vacuum test chamber. Due to the size of the chamber (diameter ≥ 2 m); the achievable lateral resolution was limited. Therefore, we decided to use a thermocamera inside the vacuum chamber, which reduces the working distance and, thus, improves the lateral resolution. Again, the thermocamera was operated in-vacuum.

We have chosen a commercial device because of its small size. Again, some vacuum-sensitive electronic parts had to be replaced. The thermocamera is surrounded by a metal housing (Fig. 10) with a ZnS window. The transmission of ZnS is $t = 0.75$ at $\lambda = 10$ µm (see Fig. 10). Other materials, e.g. KBr, KCl or NaCl would have a higher transmission ($t = 0.90$ at $\lambda = 10$ µm), but these materials are not favourable because Cl and Br are highly reactive and toxic.

The thermocamera operates in the spectral range from 7.5 µm to 13 µm. The image size is about 50 x 70 mm^2 at a working distance of 500 mm. The resolution of the camera is 160 pixels x 120 pixels. The lateral resolution is 1.5 mm. Temperature range and resolution is specified to be 0°C – 900°C and 0.1°C, respectively. The system accuracy is given to be 2 % of reading or 2°C. The overall dimension of the thermocamera (including housing) is 56 x 60 x 143 mm^3.

2.5 Retarding potential analyser

The retarding potential analyser should serve as an alternative tool to the ESMS, which was used with the AEPD1 platform. The ESMS is expensive and, therefore, its availability limited. The retarding potential analyser is used to measure the energy distribution of charged particles. It is based on measuring the ion current I in dependence on the repelling voltage U (electrostatic energy analyser). The (normalized) energy distribution is obtained by calculating the derivative of $I(U)$.

The retarding potential analyser (Fig. 11) was developed in-house with the goal to make it as small as possible while keeping the performance (signal-to-noise ratio) sufficiently high. Therefore, a grid design with 149 holes has been chosen. The device consists of two grids and an ion collector. The first grid is used for focusing the ion trajectories, the second grid for repelling secondary electrons. The ion collector is used for measuring the ion current and for repelling the ions by applying a repelling voltage V.

The ion collector has cup-shaped cavities, one for each of the 149 ion channels. The repelling voltage can be

varied between 0 V and 3000 V with accuracy better than 0.05 %. The collected ion current is transformed by a high-precision resistor into a voltage drop, which is measured by a 14-bit AD converter. The accuracy is better than 5 eV. The overall dimension of the device is 40 x 47 x 84 mm^3.

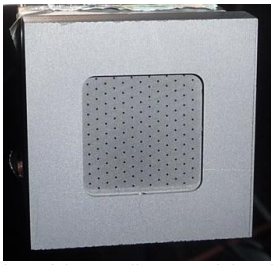

Fig. 10: Front view of the retarding potential analyser

Fig. 11. Thermocamera setup with housing (without cover and window)

2.6 Thruster

Test measurements were performed with a gridded ion thruster RIT-µX [8], which belongs to the class of radio-frequency ion thrusters (RITs). The thruster was operated with the standard propellant xenon at two operation points (see Table 1).

Table1. Summary of operation parameters of the RIT-µX at operation point 1 (OP1) and operation point 2 (OP2)

Parameter	OP1	OP2
Beam Voltage	1050 V	1700 V
Beam Current	4 mA	8 mA
Accelerator voltage	-200 V	-250 V
Nominal thrust	210 µN	540 µN

2.7 Test chamber

The tests were performed in the Jumbo test facility [9]. The tank is of cylindrical shape with a diameter of 2.6 m, a length of 6 m and a volume of 30 m^3. It is equipped with turbo and cryopumps with a total pumping speed 65.000 l/s for xenon. The base pressure is about 1 x 10^{-7} mbar.

3. Results and Discussion

Because none of the manufactures of telemicroscope, triangular laser head, pyrometer or thermocamera have specified in-vacuum operation, we first performed the principal in-vacuum tests. All devices were operated inside the vacuum for at least 48 h. The tests were successful, i.e. all devices operated properly and stably. After that, the devices were tested with firing thrusters. In the following, selected test results with the RIT-µX thruster are presented.

3.1 Telemicroscope

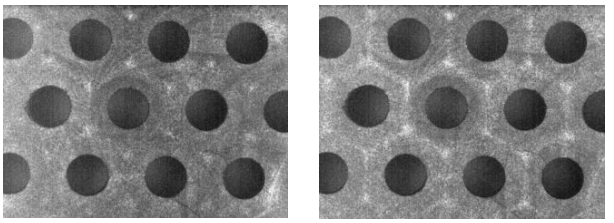

Fig. 12: Telemicroscope images of grid holes of the RIT-µX before (left)

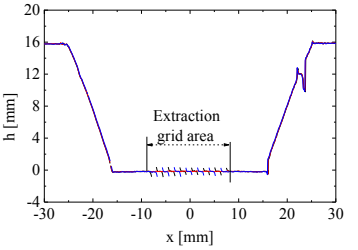

Fig. 13. Surface profile scans across the centre of the RIT-µX

and after the test campaign (right)

measured with the triangular laser head. There are three lines representing measurements from three different days

Fig. 12 shows a section of the grid (thruster is off) at the beginning and at the end of the test campaign (total duration about 100 h). The grid holes can be clearly resolved and grid hole diameter and, hence, the grid hole erosion are accessible. The diameter of the centre hole in Fig. 12 is (1.27 ± 0.02) mm for both images. The two images demonstrate the repeatability and, reliability of the measurements.

3.2 Triangular laser head

Fig. 13 shows selected surface profile scans of the RIT-µX measured on different days. A very good repeatability can be seen. The extraction grid hole area can be identified clearly and the number of holes can be seen. Doing so, the principal shape of the grid including, for instance, its radius of curvature could be measured [2,3]. The grid of the RIT-µX is flat.

However, there are experimental limitations due to the measurement principle (triangulation effect), i.e. the triangular laser head might fail in measuring steep or abrupt edges (see the sharp structures in the extraction grid area in Fig. 13).

3.3 Thermocamera

Fig. 14 shows thermocamera images of the RIT µX. The surface temperature of almost the whole thruster is imaged. The surface temperature distribution of the grid is nearly homogeneous, apart from the holes, which is caused by the fact that the temperature of the plasma chamber, which is imaged through the holes, is considerably higher than the grid surface temperature [2,3]. In Figure 15 temperature line scans across the centre of the thruster are plotted. The grid temperature was found to be (62°± 2)°C at operation point 1 and (68°± 2)°C at operation point 2.

3.4 Retarding potential analyser

Fig. 16 shows selected energy distributions measured with the retarding potential analyser at certain time steps at different days. All curves reveal a single peak, which is typical for gridded ion thrusters. The shape of the peaks is Gaussian like and very similar for all measurements. However, the peak position scatters between 1038 eV and 1046 eV. This is tentatively assigned to the fact that the peak position is mainly determined by the beam voltage but also by the plasma potential and the secondary star ground. Still, the scattering is less than 1 % of the ion energy. The width at half maximum of the peak is smaller than 20 V, which corresponds to less than 2 % of the ion energy. Ions with other energies, e.g. generated by charge exchange processes, or multiplied charged ions were not detected.

The data shows a good repeatability and reliability. However, the curves in Fig. 16 are very noisy. Therefore, the electronics needs some further improvements with regard to signal-to-noise ratio.

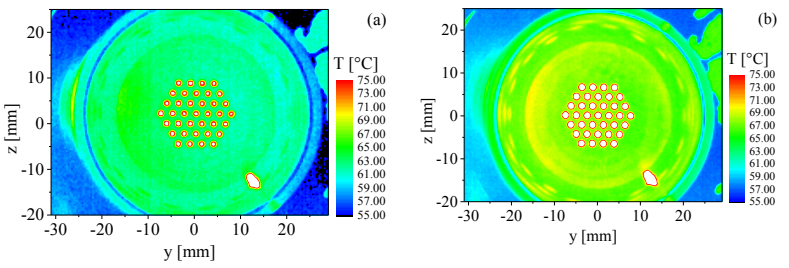

Fig. 14. Thermocamera images of the RIT-µX at OP1 (a) and OP2 (b)

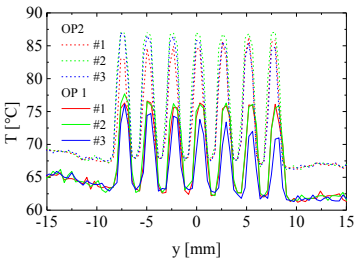

Fig. 15: Horizontal temperature scans across the centre of the RIT-µX at OP1 (solid lines) and OP2 (dashed lines) extracted from thermocamera images

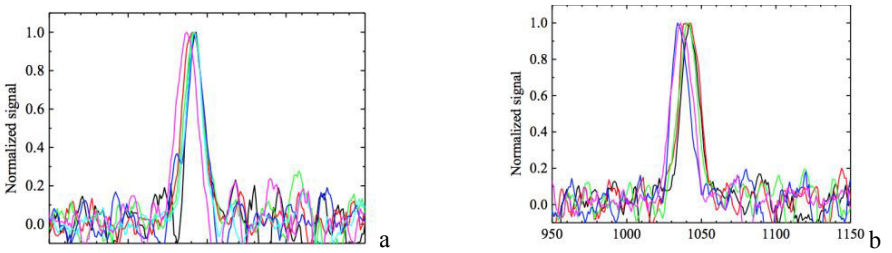

Fig. 16 Energy distributions of the RIT-µX at OP1 measured with the retarding potential analyser at two different days (day 1: a; day 2: b)

4. Conclusion

We have reported the new design of our diagnostic tools for in-situ EP thruster characterization, including probes for beam characterization (retarding potential analyser), thermal characterization (pyrometer, thermocamera) and optical inspection (telemicroscope, triangular laser head).

The designs have been improved with respect to certain problems, which were noticed with the AEPD1 platform. We are now operating all diagnostic tools, for the very first time, in-vacuum. Because of that, the size of the diagnostic tool setups could be reduced considerably, which reduces the interaction between the energetic particles beam of the thruster with the diagnostics, and the risk of a vacuum breakdown is eliminated completely. We have shown that the tools operate well in the vacuum environment with a firing thruster, even though they are not specified for in-vacuum operation, and provide reliable and reproducible results.

In the next step all diagnostic tools need to be evaluated thoroughly with respect to possible sources of uncertainty. This is, especially, important when going to provide standardized diagnostic tools. Standardization is a major issue [5,6], even though suitable standards are missing for most of the diagnostic tools.

5. Acknowledgement

We acknowledge financial support from the European Space Research and Technology Centre (ESTEC) of the European Space Agency (ESA) within project 4000107451/12/NL/RA. The authors are greatly indebted to R. Woyciechowski, M. Müller, S. Daum (all Leibniz-Institute of Surface Modification), R. Kukies (Airbus Defence & Space), P. Köhler, W. Gärtner, U. Bachmann (all Justus-Liebig-Universität Gießen) for technical support.

References

[1] C. Bundesmann, M. Tartz, F. Scholze, H.J. Leiter, F. Scortecci, R.Y. Gnizdor, H. Neumann, Note: An advanced in situ diagnostic system for characterization of electric propulsion thrusters and ion beam sources, Rev. Sci. Instrum. 81 (2010) 046106.

[2] C. Bundesmann, M. Tartz, F. Scholze, H. Neumann, H.J. Leiter, F. Scortecci, D. Feili, P.−E. Frigot, J. Gonzalez del Amo, In-situ temperature, grid curvature, erosion, beam and plasma characterization of a gridded ion thruster RIT 22, in Proceedings of the 31st International Electric Propulsion Conference, Ann Arbor, 2009, Paper IEPC-2009-160.

[3] C. Bundesmann, M. Tartz, F. Scholze, H. Neumann, H.J. Leiter, F. Scortecci, In situ Thermal Characterization of the Accelerator Grid of an Ion Thruster, J. Propul. Power 27 (2011) 532.

[4] C. Bundesmann, M. Tartz, F. Scholze, H. Neumann, F. Scortecci, S. Scaranzin, P.−E. Frigot, J. Gonzalez del Amo, R.Y. Gnizdor, In situ temperature, erosion, beam and plasma characterization of a SPT-100D EM1 with an advanced electric propulsion diagnostic system, in Proceedings of the 31st International Electric Propulsion Conference, Ann Arbor, 2009, Paper IEPC-2009-141.

[5] D. Pagano, F. Scortecci, C. Bundesmann, C. Eichhorn, F. Scholze, H. Neumann, H. Leiter, H. Kersten, S. Gauter, R. Wiese, R. Blott, P.J. Klar, K. Holste, B. Meyer, S. Mazouffre, A. Bulit, J. Gonzales del Amo, Qualification of the AEPD System as a Standard On-Ground Tool for Electric Propulsion Thrusters, in Proceedings of the 34th International Electric Propulsion Conference, Hyogo-Kobe, 2015, Paper IEPC-2015-363.

[6] C. Bundesmann, C. Eichhorn, F. Scholze, D. Spemann, H. Neumann, D. Pagano, S. Scaranzin, F. Scortecci, H.J. Leiter, S. Gauter, R. Wiese, H. Kersten, K. Holste, P. Köhler, P.J. Klar, S. Mazouffre, R. Blott, A. Bulit, K. Dannenmayer, J. Gonzales del Amo, Qualification of the AEPD system as a Standard On-ground Tool for Electric Propulsion Thrusters – Status and Perspectives, in Proceedings of 5th Space Propulsion Conference, Roma, 2016, Paper SP2016_3124997.

[7] C. Bundesmann, C. Eichhorn, F. Scholze, H. Neumann, H.J. Leiter, F. Scortecci, Electric Propulsion Thruster Diagnostic Activities at IOM, in Proceedings of the 34th International Electric Propulsion Conference, Hyogo-Kobe, 2015, Paper IEPC-2015-392.

[8] C. Altmann, H. Leiter, R. Kukies, The RIT µX Miniaturized Ion Engine System way to TRL 5, in Proceedings of the 34th International Electric Propulsion Conference, Hyogo-Kobe, 2015, Paper IEPC-2015-274.

[9] P.J. Klar, K. Hannemann, U. Ricklefs, H. Leiter, Overview of the research activities of the RITSAT-project, in Proceedings of the 34th International Electric Propulsion Conference, Hyogo-Kobe, 2015, Paper IEPC-2015-89.